



Cavitation bubble collapse in a vicinity of a liquid-liquid interface – Basic research into emulsification process

Uroš Orthaber, Jure Zevnik, Rok Petkovšek, Matevž Dular*

Faculty of Mechanical Engineering, University of Ljubljana, Askerceva 6, 1000 Ljubljana, SI, Slovenia

ARTICLE INFO

Keywords:

Cavitation
Liquid-liquid interface
Bubble
Oil
Emulsion
Simulation

ABSTRACT

The initial motivation for the study was to gain deeper understanding into the background of emulsion preparation by ultrasound (cavitation). In our previous work (Perdih et al., 2019) we observed rich phenomena occurring near the liquid-liquid interface which was exposed to ultrasonic cavitation. Although numerous studies of bubble dynamics in different environments (presence of free surface, solid body, shear flow and even variable gravity field) exist, one can find almost no reports on the interaction of a bubble with a liquid-liquid interface. In the present work we conducted a number of experiments where single cavitation bubble dynamics was observed on each side of the oil-water interface. These were accompanied by corresponding simulations. We investigated the details of bubble interface interaction (deformation, penetration). As predicted, by the anisotropy parameter the bubble always jets toward the interface if it grows in the lighter liquid and correspondingly away from the interface if it is initiated inside the denser liquid. We extended the analysis to the relationships of various bubble characteristics and the anisotropy parameter.

Finally, based on the present and our previous study (Perdih et al., 2019), we offer new insights into the physics of ultrasonic emulsification process.

1. Introduction

Cavitation is a physical phenomenon accompanied by chemical processes that can occur in liquids. The phenomenon encompasses the growth and collapse of vaporous or gaseous cavities in a liquid as a consequence of the local pressure drop and its recovery, respectively.

The vapor structures are unstable, and when they reach a region of increased pressure, they often collapse violently. As a result, strong shear flows [2], jets [3], high local temperatures [4], shock waves [5], rapid depressurization [6] and supersonic flow [7] can appear. Cavitation has long been regarded as an undesirable phenomenon as it causes noise, vibration and erosion to the machinery, but in the past decade, studies have shown that there is a great potential to utilize cavitation in various important applications in the fields of biology [8], chemistry [9], medicine [10], in environmental protection [11,12], in liquid food applications such as beer [13], for the intensification of various other chemical and physical processes [14], and also for preparation of emulsions [1]. In the latter paper [1], we demonstrated that for the case of ultrasonically induced process of formation of oil in water (O/W) emulsion proves to be more complicated than previously thought. Before the final O/W emulsion is formed, firstly a water in oil (W/O) emulsion forms inside the bulk oil phase. W/O droplets are later

separated from the bulk oil phase and undergo further break down under the influence of ultrasonic waves, and after all these steps are repeated a few times a true O/W emulsion develops. Despite new insight of the process was gained some open questions remained, which we were unable to answer when observing multiple acoustically generated bubbles. One such question is the physics behind the first step – formation of W/O emulsion – is it really the jetting of the bubble into the oil phase or is the process governed by the acoustic streaming [15,16]?

A partial and theoretical answer can be found in the recent work by Suponnen et al. [17], where they reviewed micro-jets of different origins, scales and appearances, and proposed a unified framework to describe their dynamics by using an anisotropy parameter. Unfortunately, they only experimentally evaluated this parameter against disturbances of gravity and nearby boundaries (solid and free), but not for the case of liquid-liquid interface, which is essential for explaining the emulsification process.

Even on the simplest level – a single cavitation bubble – can give a wide ensemble of phenomena such as splitting [18], shock wave emission [19], splashing [20], luminescence [21], jetting [17], the later – jetting – being one of the more interesting ones (also in applications of ultrasonically induced emulsification process). If the bubble is exposed

* Corresponding author.

E-mail address: matevz.dular@fs.uni-lj.si (M. Dular).

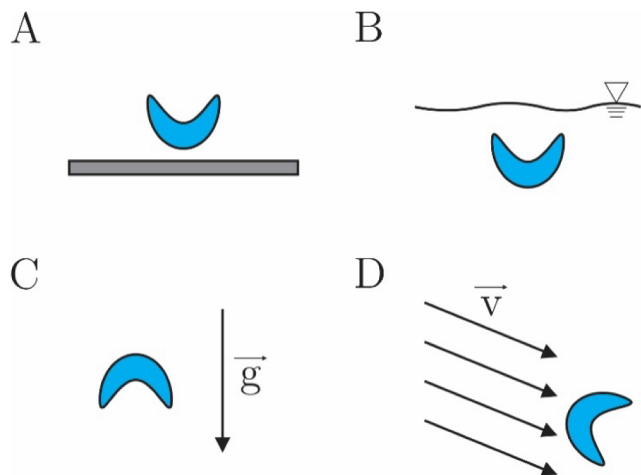


Fig. 1. Bubble collapse and jetting inside an anisotropic pressure field, which results from different causes (A – presence of rigid surface, B – presence of free surface, C – presence of gravity field, D – presence of shear flow).

to an asymmetrical pressure field a jet will normally occur as it collapses. This can occur in the case of various anisotropy drivers, such as in a presence of a gravitational field, nearby boundaries, other bubbles, stationary potential flow. Fig. 1 shows typical jetting inside an anisotropic pressure field (with different origins).

Following the work of Supponen et al. [17], the researchers quantified the jet-driving pressure anisotropy with a dimensionless vector parameter ζ , which acts as a dimensionless measure of liquid momentum during the aspherical bubble collapse and is in its general form defined as:

$$\zeta = -\nabla p R_{\max} \Delta p^{-1} \quad (1)$$

Here, ∇p represents the pressure gradient that drives the jet, R_{\max} the maximum bubble radius and Δp the collapse driving pressure, defined as a difference between the pressure at infinity and the vapor pressure. In other words, parameter ζ represents a dimensionless version of the Kelvin impulse [22–24], and is defined for various types of boundaries and pressure gradients. A general form of the anisotropy parameter in a bounded environment, where gravity is absent can be written as [17]:

$$\zeta = 0.195 \cdot \gamma^{-2} \frac{(\rho_1 - \rho_2)}{(\rho_1 + \rho_2)} \mathbf{n} \quad (2)$$

with index 1 referring to the substance of bubble origin and index 2 referring to the nearby substance. ρ is the corresponding liquid density and \mathbf{n} is the normal unit vector on the surface pointing to the cavity centre. γ is defined as a nondimensional distance of the bubble centre (at its maximal size) from the boundary (solid, surface, interface):

$$\gamma = \frac{h}{R_{\max}} \quad (3)$$

One can note from Eq. (2), that if $\rho_1 \ll \rho_2$ we deal with the problem of bubble near a solid (rigid) boundary. On the other hand, when $\rho_1 \gg \rho_2$, the case describes a bubble near a free surface.

Bubble collapse in the vicinity of a rigid surface, free surface and even gravity field was extensively investigated in the past [18–22,25–28]. On the other hand the liquid-liquid interface received much less attention – a sole experimental paper on the topic was published in 1980 by Chahine & Bovis [29]. They discuss that the direction of the jet is mainly dependent on the nondimensional distance of the bubble from the interface γ . But this conclusion bases only on experiments with approximately $\rho_1 \approx 1.2 \cdot \rho_2$.

In the present paper we focus on the dynamics of a bubble, which is collapsing in the vicinity of a liquid-liquid, namely water-oil, interface. We performed experiments, where cavitation bubble was generated by

a laser pulse on both sides of the water and oil interface, in other words – cases with $\rho_1 > \rho_2$ and $\rho_1 < \rho_2$ at different nondimensional distance are considered. In addition, the experiments are complemented by simulations.

The investigation is extremely important, due to its applicability to emulsification process, for which we have shown in our previous work [1] using acoustic cavitation, that it can be described by a number of consequential steps, the first being the interaction between a single cavitation bubble and the liquid-liquid interface.

2. Methodology

Due to the complex nature of the phenomena, we approach the investigation from both experimental and numerical aspects. High speed video and computational fluid dynamics are the main tools used in the present study.

2.1. Experimental approach

In order to study cavitation bubble dynamics in the vicinity of water-oil interface, experimental setup was prepared, which enabled high-speed recording of this phenomenon for two cases: in the first case the cavitation bubble was produced in water and in the second case the bubble was produced in oil. Distance between bubble and water-oil interface was varied so that parameter γ assumed values between 0.01 and 1.5, where γ is defined as the ratio of the distance between the centre of the bubble from the interface to the maximum bubble radius (Eq. (3)).

The water-oil interface was produced by submerging a large droplet of sunflower oil attached onto a vertical metal holder in a water-filled glass tank. Oil droplet was an order of magnitude larger than the cavitation bubble. This is essential to minimize the effect of the curvature of the interface on the bubble dynamics. Previous experiments on vaguely similar cases show us that the curvature of the interface is only important if it is comparable to the one of the bubble – Tomita et al. [30] experimented with bubbles near highly curved rigid surfaces, which is similar to the present case where the bubble is created in water near an oil droplet. They note that the bubble life will be shortened if it grows and collapses in the vicinity of a convex rigid surface with similar curvature as the bubble wall (at its maximal size). In the present case the ratio of curvatures is about 10:1, and the wall is not rigid at all. Hence, such effects are much smaller and likely negligible. In an opposite case, where the bubble is created inside the oil droplet the influence is similar. Farhat et al. [31] conducted experiments where a bubble was created inside a water droplet. They also noticed a small deviation in the bubble collapse time, which was shortened, compared to the Rayleigh collapse time. However, the maximal bubble was very large compared to the droplet size – about 1:2. Again in the present case the ratio is 1:10, and such effects are much smaller and likely negligible. Finally, in our previous paper on emulsification [1] we also considered a case with a flat oil water interface and an oil droplet with a curved interface. The dynamics of emulsification the two cases was very similar, which again leads us to an assumption that the effect of curvature in the present experiments is negligible.

Oil droplet was located in the center of the water tank with dimensions $10 \times 5 \times 5$ cm, approximately 2.5 cm below the water surface. Cavitation bubble was produced with a tightly focused laser beam as shown in the Fig. 2.

Laser used to produce cavitation bubble was a Q-switched Nd:YAG laser with a wavelength of 1064 nm and a pulse duration of approximately 5 ns. The energy was set to 13 mJ, which corresponds to pulse peak power of > 2 MW. Optical system was used to expand the laser beam, which was then tightly focused, having a numerical aperture of approximately 0.25. This is sufficient to cause ionization in the liquid environment, thus leading to the development of a cavitation bubble.

Cavitation bubble dynamics in the vicinity of water-oil interface

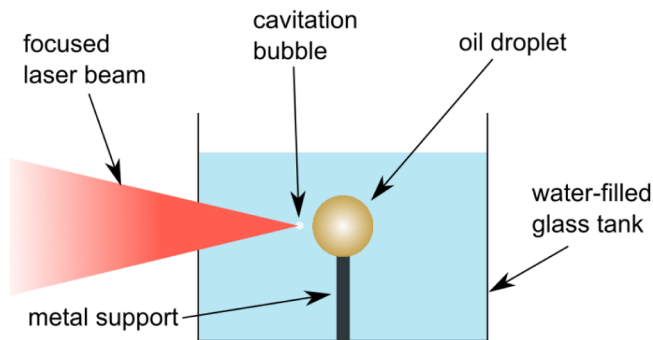


Fig. 2. Experimental setup – detail (view from the side, case where bubble was formed inside water).

was recorded by a high-speed camera Photron Fastcam SA-Z with a frame rate of 100,000 fps, while LED light source Ryobi One + (50000 lm) served as an illumination source.

2.2. Numerical approach

To achieve a further insight into the considered phenomenon, an axisymmetric numerical model was set up in a commercial solver Fluent 20.1 [32] that is based on the finite volume method. The interface between the phases was captured by the volume of fluid method, which has already been shown to successfully resolve various cases of aspherical bubble dynamics, such as in vicinity of a rigid wall [33,34], in a gravity field [35], bubble pair interaction [36], etc.

The gas phase is modelled as a non-condensable ideal gas without considering the mass transfer mechanisms and bubble's vapor content. Both liquid phases, water and vegetable oil, are modelled as compressible with Tait's equation of state with reference densities of $\rho_w = 998.2 \text{ kg/m}^3$ and $\rho_o = 918.8 \text{ kg/m}^3$ at the ambient pressure of $p_\infty = 101325 \text{ Pa}$. Density exponents of both liquids were taken to be $n_w = 7.15$ and of $n_o = 7$, whereas their reference bulk moduli were set to $K_w = 2.2 \text{ GPa}$ and $K_o = 1.4 \text{ GPa}$. Viscosity of all phases is included with dynamic viscosity of gas, water and oil: $\mu_g = 1.8 \times 10^{-5} \text{ Pa}\cdot\text{s}$, $\mu_w = 10^{-3} \text{ Pa}\cdot\text{s}$ and $\mu_o = 4.91 \times 10^{-2} \text{ Pa}\cdot\text{s}$, respectively. On the other hand, the effects of surface tension are neglected, since the Weber's number for liquid jets considered here is in the order of 10^3 to 10^6 and therefore suggests a minor role on bubble dynamics at this scale. This can be further supported by recent findings of Lechner et al. [37], who came to similar conclusions when performing simulations of laser induced bubbles close to a rigid wall.

A scheme of the considered numerical setup can be seen in Fig. 3.

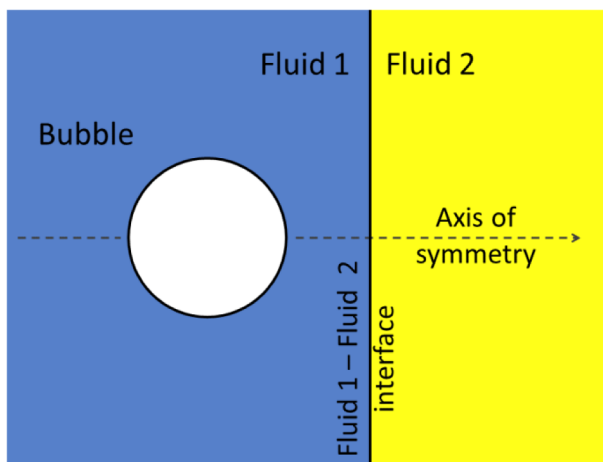


Fig. 3. Scheme of the numerical setup.

Two different numerical grid types were used in this study, an o-type grid with a resolution of 360 cells per perimeter and an orthogonal grid with a constant resolution of $10 \mu\text{m}$ in the bubble domain, which gradually coarsens outwards. The former was used for the evaluation of a spherically symmetric case and for bubbles very close to the water-oil interface ($\gamma = 0.2$), whereas the latter was utilized for all other cases with larger values of γ , since it resulted in a more stable water-oil interface development. For all cases, the size of the computational domain was set to $100R_{\text{max}}$ to minimize the effects of boundary conditions. Additionally, the grid was automatically refined at the interface of the phases before each time step, based on the gradient of volume fractions. Up to three levels of refinement were permitted to achieve a spatial resolution of the bubble domain in the order of $1 \mu\text{m}$.

Since the behaviour of bubbles after the first collapse is important in the present study, initializing the bubble with an overpressure is not sufficient, as the obtained rebounds are much too large compared to the experimental data. This discrepancy arises due to neglect of mass transfer mechanisms, namely the vapor condensation upon the first bubble collapse. According to Akhatov et al. [38], who modelled spherically symmetric laser induced bubble collapse, vapor condensation at the bubble surface is inversely proportional to the initial amount of the non-condensable gas, which consequently greatly influences the magnitude of the maximum rebound radius. According to the recent research, aspherical bubble dynamics can be captured very well even by modelling bubble contents solely as a non-condensable gas. To match the bubble behaviour after the first collapse to the experimental data, other authors so far either supplied the bubble with a time dependent excess pressure at the beginning of the simulation [33] or gradually reduced the bubble contents when it reached its maximum size [37]. In our case, we take a different approach by initializing both the pressure and velocity field in the computational domain, to match the experimental data until the second bubble collapse. We obtained a relatively good match by using the following expressions to initialize the velocity field (Eq. (4)),

$$u_0(r) = \begin{cases} \dot{R}_0 \left(\frac{r}{R_0} \right)^2 & \text{for } r \leq R_0, \\ \dot{R}_0 \left(\frac{R_0}{r} \right)^2 & \text{for } r > R_0, \end{cases} \quad (4)$$

and the pressure field (Eq. (5)),

$$p_0(r) = \begin{cases} p_\infty \left(\frac{R_{eq}}{R_0} \right)^{3k} & \text{for } r \leq R_0, \\ p_\infty + \frac{R_0}{r} \left(p_\infty \left(\frac{R_{eq}}{R_0} \right)^{3k} - \frac{4\mu\dot{R}_0}{R_0} - p_\infty \right) + \frac{1}{2}\dot{R}_0^2 & \text{for } r > R_0 \\ \rho \frac{R_0}{r} \left(1 - \frac{R_0^3}{r^3} \right) & \end{cases} \quad (5)$$

Here R_0 represents the initial bubble radius, \dot{R}_0 the initial bubble wall velocity, r a distance from the bubble's center to a given point, p_∞ the ambient pressure, R_{eq} the equilibrium bubble radius, k the adiabatic exponent of gas, considered as 1.4, μ the dynamic viscosity, and ρ density of the surrounding liquid. As our main interest lies in capturing the general bubble shape progression, we omit the modelling of actual processes behind laser-induced bubble formation (dielectric breakdown, plasma formation and shock wave emission), and start all simulations for an already expanding bubble with the initial bubble radius of $R_0 = R_{\text{max}}/6.25$. This value translates to an initialized bubble in the case of the smallest numerically considered gamma still being reasonably far away from the water-oil interface to neglect its deformation up to this point. Since k , μ and ρ are known properties, one can see that after determining the initial bubble radius R_0 , two parameters remain to determine the bubble dynamics: the initial velocity of the bubble wall \dot{R}_0 , which predominantly affects its first expansion, and the equilibrium radius R_{eq} , which mostly affects the intensity of the collapse and the following rebound. One might notice that the

employed initial conditions are related to the case of an unbounded bubble in an infinite incompressible liquid. Based on the results of preliminary simulations, we decided to omit the last term in Eqn. (5), $\frac{1}{2}\dot{R}_0^2 \rho_r \left(1 - \frac{R_0^3}{r^3}\right)$, which accounts for the already developed velocity field in the surrounding liquid. The reason for this is the fact that we obtained better results this way, since the inclusion of this term resulted in an overextension of the state, where the bubble was around its maximum size.

As mentioned before, parameters \dot{R}_0 and R_{eq} remain to be determined, which can be done by the trial and error approach to fit the obtained results to the available experimental data. In our case, \dot{R}_0 and R_{eq} were fitted to the experimental case, where the bubble was created either in water ($R_{max} = 850 \mu\text{m}$) or oil ($R_{max} = 945 \mu\text{m}$), far from their interface ($\gamma \gg 1$). As mentioned before, the obtained numerical results can only be relevant until the second bubble collapse, as the following rebounds tend to be overpredicted due to neglect of mass transfer mechanisms. The obtained initial parameters were then kept constant within each simulation set and are $\dot{R}_0 = 136 \text{ m/s}$, $R_{eq} = 120 \mu\text{m}$ for bubbles in water and $\dot{R}_0 = 127 \text{ m/s}$, $R_{eq} = 306 \mu\text{m}$ for bubbles in oil, respectively. A comparison between experimental and numerical results for both cases is given in Fig. 4.

Even though there is a relatively good match for both cases, a temporal discrepancy can be observed between the experimental and numerical results for the initial bubble growth phase. It is likely that the cause is a rather arbitrary initialization of the numerical simulations, which assumes an already developed flow field around the bubble, and does not account for the actual processes of a laser-induced bubble formation (dielectric breakdown, plasma formation and shock wave emission).

3. Results

We investigated the dynamics of bubbles on each side of the liquid-liquid interface. The energy input at the laser breakdown was constant, as mentioned in Section 2.1, while coefficient γ was varied on each side of the water-oil interface. Anisotropy parameter corresponding to listed γ coefficients spans from 0.2 to -8.1 , with the corresponding ζ value being stated in the beginning of each of the following subsections.

Each frame in recorded sequences as well as in simulated sequences is assigned a specific time in microseconds, with the first frame always set to zero. Time zero does not represent any specific event in bubble dynamics and is simply applied to the frame in the recorded sequence, in which a cavitation bubble was first observed. The following frames are assigned time values corresponding to the high-speed camera frame rate. It can be observed from the recorded sequences that the largest bubble size appears always at $70 \mu\text{s}$, meaning that the bubble oscillation period differs by no more than $\pm 5 \mu\text{s}$ between different recorded

sequences.

Simulated sequences were constructed in such a way that the frame with the largest bubble size was set to $70 \mu\text{s}$ to match the frame with recorded sequence, while other frames in the simulated sequence positioned at time intervals corresponding to camera frame rate were picked from the simulation and assigned appropriate time value with respect to the $70 \mu\text{s}$ frame. Since the moment of maximum bubble size can be determined from the experiment with an error of $\pm 5 \mu\text{s}$, this is also the error by which the frames in simulated sequences were picked from simulation.

3.1. Bubble collapse far from the liquid-liquid interface ($\gamma = 1.5$, $\zeta = \pm 0.0036$)

3.1.1. Bubble in water

Fig. 5 shows experimental observation of a bubble which was generated in water at $\gamma = 1.5$, $\zeta = 0.0036$, while Fig. 6 shows the corresponding simulated sequence.

Experimentally observed cavitation bubble dynamics at $\gamma = 1.5$ resembles dynamics of a bubble in an infinite liquid, since oil-water interface has no visible influence on bubble growth and collapse cycle. It can be noticed however, that the bubble is split into two parts upon collapsing, which can be attributed to the asymmetry in bubble shape. Bubble dimension is greater in vertical as opposed to horizontal direction, a result of elongated laser-induced plasma shape, which is generated during the optical breakdown. The collapse is thus stronger in vertical direction, which leads to the splitting of the bubble. Consequently, two liquid jets originating in the centre of the former bubble pierce both newly appeared bubbles, one directed towards and the other away from the water-oil interface. This is a result of a high-pressure gradient in radial direction from the centre of the split bubble outwards and has seemingly nothing to do with the water-oil interface.

Simulated sequence in Fig. 6 shows slightly different behaviour. In the absence of experimental imperfections, a jet is developed in the final collapse stage of the cavitation bubble with jet being directed away from the water-oil interface. The correlation with the recorded sequence is small. It can be noticed however in Fig. 5 that the jet through the left part of the split bubble is slightly stronger, which could indicate the influence of the interface. Any particular bubble behaviour due to the water-oil interface in this case is greatly overshadowed by the mentioned imperfect circumstances, since the distance from the interface is too large for it to cause significant observable effect.

The described case at $\gamma = 1.5$ and $\zeta = 0.0036$ is right at the boundary between weak jets and intermediate jets, as it was defined by Supponen et al. [17]. This may also be the reason that we do not see the jet in experiment (Fig. 5), but it is evident in simulation (Fig. 6). We believe that the issue is not only in the not ideally executed experiment, but also in the limitations of the equipment (camera framerate and

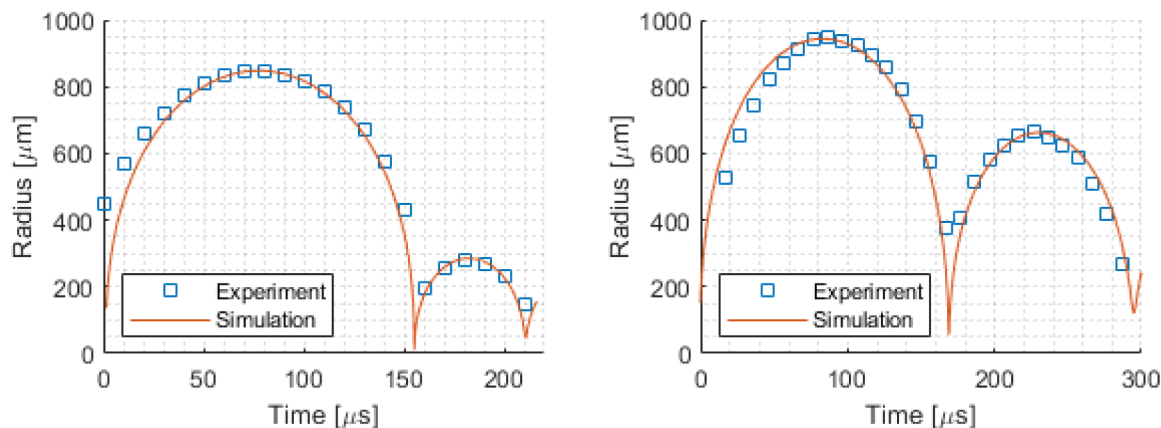


Fig. 4. Bubble radius development and experimental results for an unbounded bubble in water (left) and oil (right).

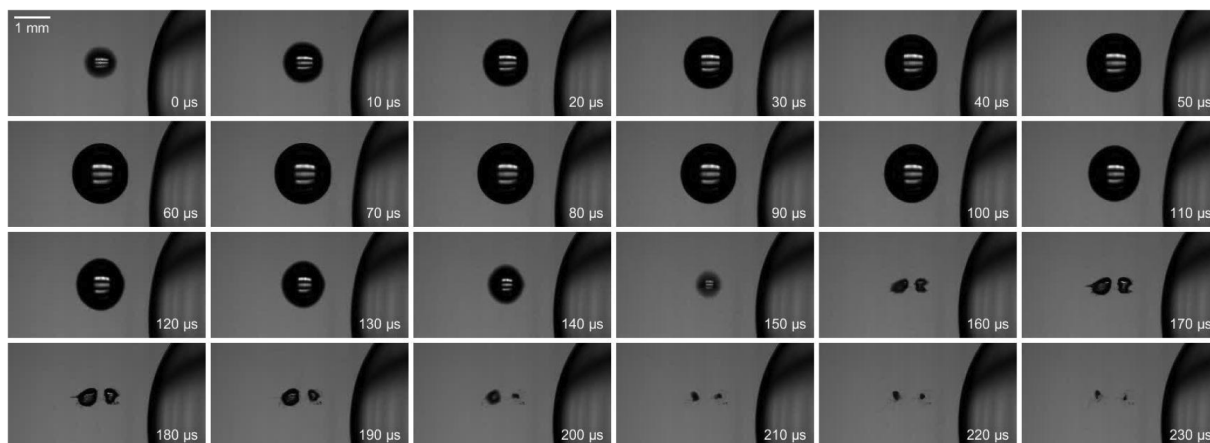


Fig. 5. Bubble evolution in water at $\gamma = 1.5$ and $\zeta = 0.0036$, experimental observation.

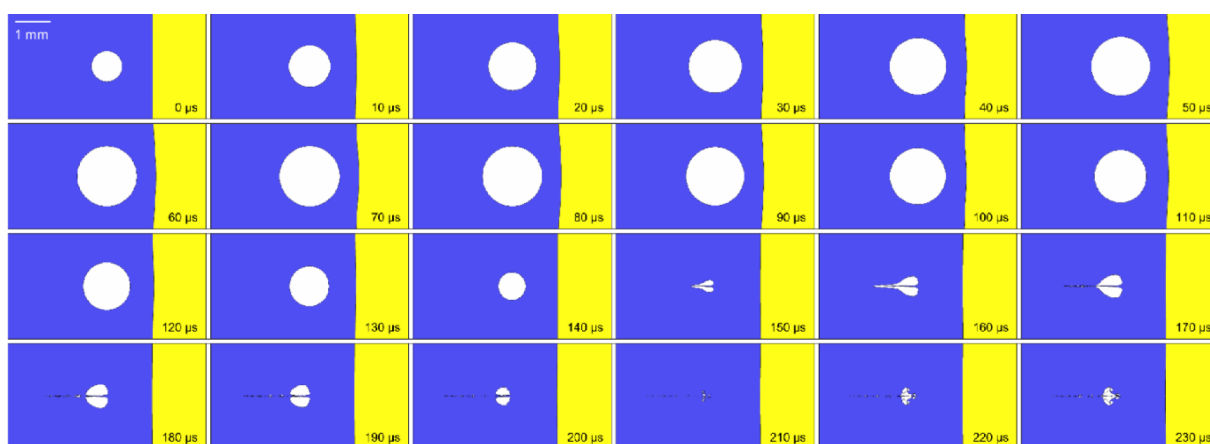


Fig. 6. Bubble evolution in water at $\gamma = 1.5$ and $\zeta = 0.0036$, numerical simulation.

resolution).

3.1.2. Bubble in oil

The bubble in Fig. 7 was generated in oil at $\gamma = 1.5$, $\zeta = -0.0036$. Fig. 7 shows experimental observation, while Fig. 8 shows the corresponding simulated sequence.

In case of cavitation bubble generated in the oil part of the water-oil interface at $\gamma = 1.5$ no significant influence of the boundary on the bubble dynamics can be noticed either from the experimental sequence. This time however, the bubble is not split into two parts upon collapsing. The reason may lie in different physical properties of oil as opposed to water (viscosity, density, surface tension). In frame at 160 μ s a

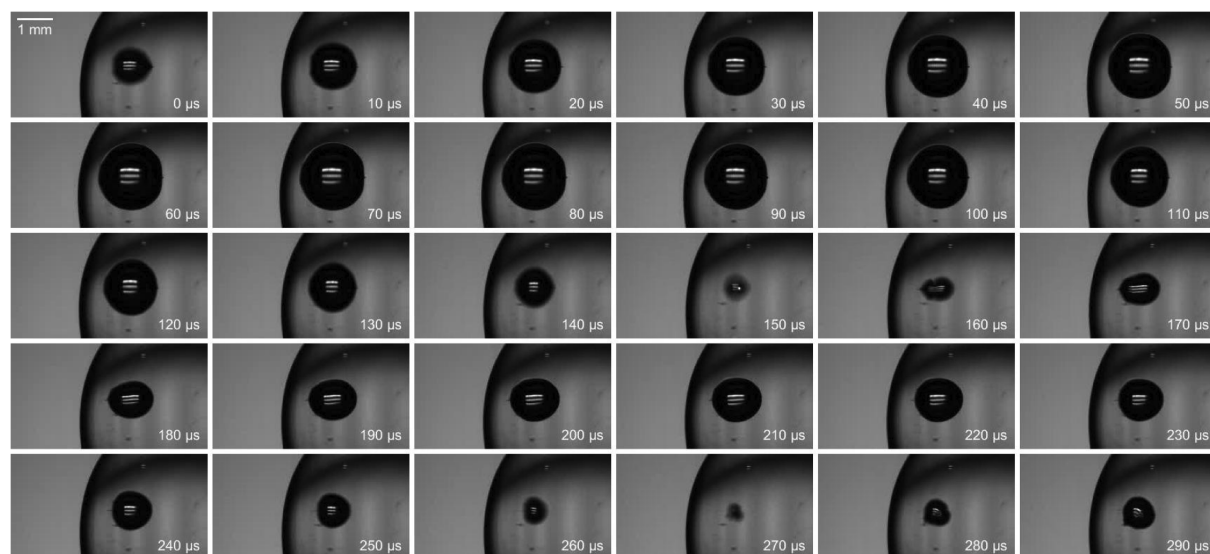


Fig. 7. Bubble evolution in oil at $\gamma = 1.5$ and $\zeta = -0.0036$, experimental observation.

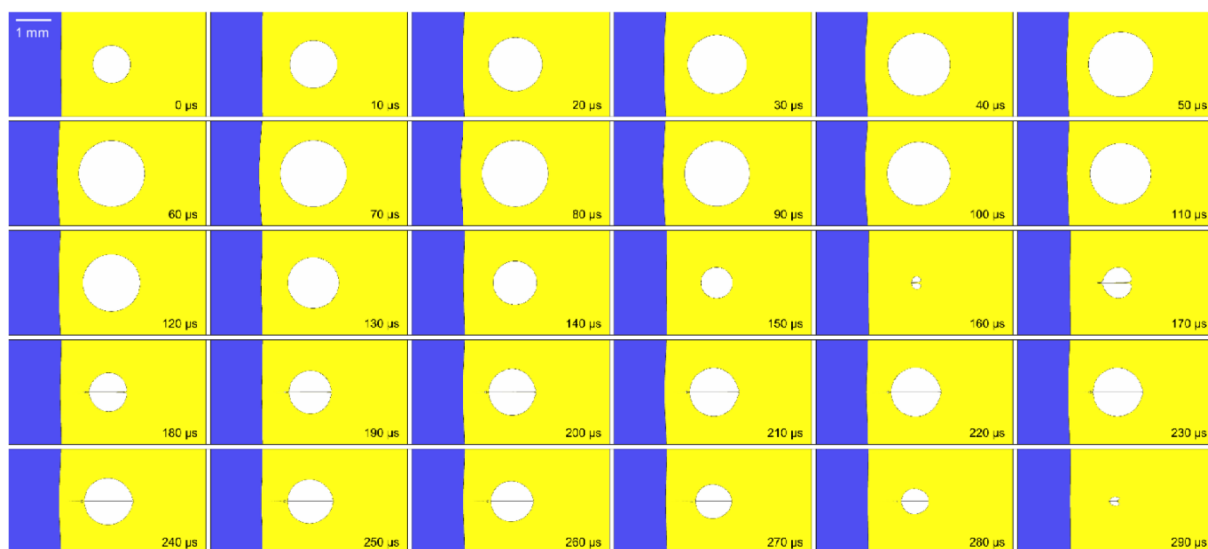


Fig. 8. Bubble evolution in oil at $\gamma = 1.5$ and $\zeta = -0.0036$, numerical simulation.

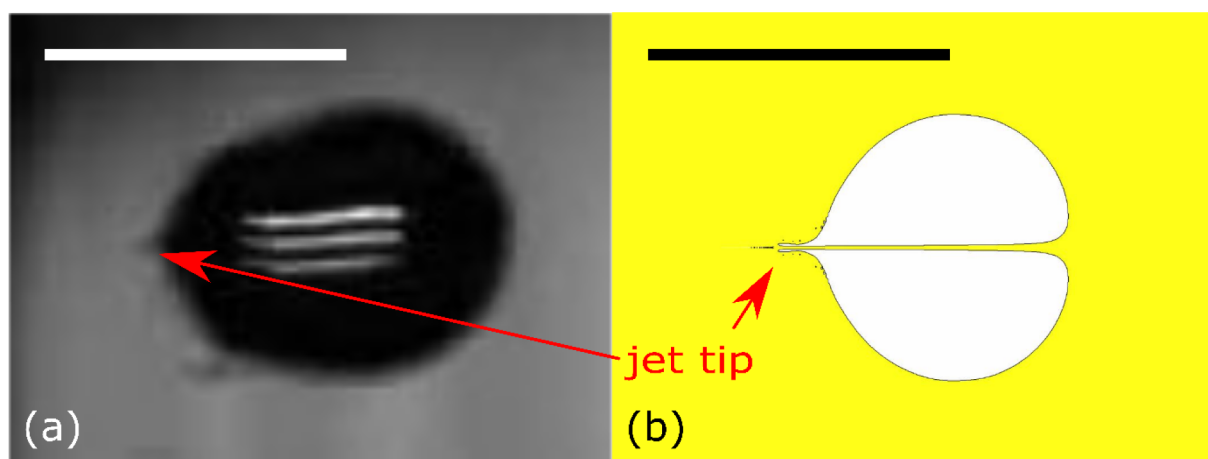


Fig. 9. (a) Experimental detail of a jet-pierced bubble at 170 μs of the recorded sequence and (b) numerical simulation showing jet phenomena as well.

possible evidence of bubble splitting is noticed, which could occur sometimes between $t = 150 \mu\text{s}$ and $t = 160 \mu\text{s}$. After this time, the bubble reclaims approximately spherical shape during second growth phase. Also, a small jet seems to appear at frame 160 μs and at the later times, which is indicated by a small sharp tip on the left side of the cavitation bubble. Numerical simulation supports this observation as seen in Fig. 8 in frame 170 μs and following frames. Due to a large distance of the bubble from the boundary, the jet's strength is relatively weak and only suffices for jet to pierce the opposing bubble wall. Fig. 9a shows recorded frame showing supposed jet piercing the bubble from the right, while Fig. 9b supports this hypothesis via numerical simulation.

3.2. Bubble collapse close to the liquid–liquid interface ($\gamma = 0.7$, $\zeta = \pm 0.016$)

3.2.1. Bubble in water

The bubble in Fig. 10 was generated in water at $\gamma = 0.7$, $\zeta = 0.016$. Fig. 11 shows the corresponding numerical simulation sequence.

A liquid jet pierces cavitation bubble in the direction away from the water–oil interface in the final phase of bubble collapse, which is especially evident from frames 160 μs to 200 μs in Fig. 10. In this case bubble splitting still occurs due to imperfect optical breakdown conditions as evident from frame 170 μs , however the left part of the split

bubble is now much larger with a more significant jet, due to the influence of the water–oil interface. The part of the split bubble on the right also experiences jetting, but much less significant. This detail is shown in Fig. 12a, while Fig. 12b depicts corresponding frame from numerical simulation. In Fig. 12b one can also observe a small residual deformation of the oil–water interface. The balance between both split parts of the bubble as shown in Fig. 12a is in favour of the left bubble since the jetting has two contributions, the nearby boundary and the asymmetric collapse.

3.2.2. Bubble in oil

The bubble in Fig. 13 was generated in oil at $\gamma = 0.5$, $\zeta = -0.016$. Fig. 14 shows the corresponding numerical simulation sequence.

A liquid jet in the direction towards the water–oil interface is visible during bubble collapse at 150 μs (Fig. 13). Jet impact creates a bump at the boundary, which persists all the way through the recorded sequence and disappears only after the cavitation bubble is long gone (not visible in this recorded sequence). The distance from the bubble to the water–oil interface is too great for liquid jet to pierce through. A small bump can also be noticed on the cavitation bubble surface on the right side, which persists throughout the entire sequence. This is a result of a laser-induced plasma, which is of conical shape with a sharp tip in the end. This shape roughly translates to the shape of the cavitation bubble.

Asymmetric behaviour can be also seen from the numerical results

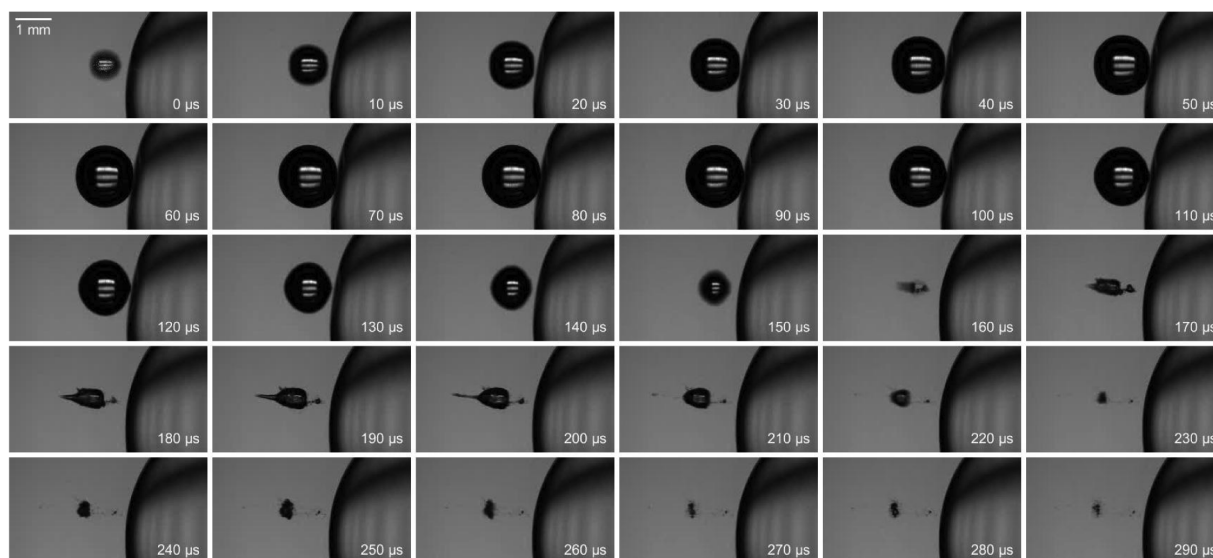


Fig. 10. Bubble evolution in water at $\gamma = 0.7$. and $\zeta = 0.016$, experimental observation.

in Fig. 14, although it only becomes apparent in the final stages of the collapse and the following rebound (frames corresponding to 160 μs and above), when a thin jet is developed towards the oil-water interface. In Fig. 15a one can notice that the small bump at the water-oil interface, which is produced by the jet from the right, almost separates from the interface. It appears that the rising bump narrows in the middle and a small droplet almost leaves the oil surface. It however blends back with the oil phase, since the jetting force is too weak to perforate the interface. This effect is also confirmed by numerical simulations as seen in Fig. 15b. The onset of liquid jet penetration of the interface can be considered as one of the more important mechanisms of cavitation assisted emulsification process.

3.3. Bubble collapse very close to the liquid-liquid interface ($\gamma = 0.5$, $\zeta = \pm 0.032$)

3.3.1. Bubble in water

The bubble in Fig. 16 was generated in water at $\gamma = 0.5$, $\zeta = 0.032$. Fig. 17 shows the corresponding numerical simulation sequence.

The sequence (Fig. 16) is quite similar to the one at $\gamma = 0.7$ with cavitation bubble in the water side of the water-oil interface (Fig. 13). It can be most clearly seen from this recording sequence, by comparing frames at 150 μs and 210 μs for example, that the centre of the bubble moves away from the oil-water interface. The bubble moves away from

the interface also after the second collapse as seen at frames 240 μs to 290 μs . This is also confirmed by numerical simulation (Fig. 17).

3.3.2. Bubble in oil

The bubble in Fig. 18 was generated in oil at $\gamma = 0.5$, $\zeta = -0.032$. Fig. 19 shows the corresponding numerical simulation sequence.

The bubble evolution is again similar to the case of bubble in the oil phase at $\gamma = 0.7$. In the case of $\gamma = 0.5$ however, the liquid jet penetrates through the oil-water interface, as seen in frame at 150 μs . Due to the pressure gradient, the cavitation bubble is pulled through the boundary and continues the growth and collapse cycle in the water phase of the oil-water interface. Upon second collapse, which occurs in the water, liquid jet is directed away from the oil-water interface. This jet is similar to those from the recordings of bubble generated in water at $\gamma = 0.7$, 0.5 and 0.2 with respect to the boundary. The bubble surroundings however appear quite smeared as a result of tiny oil droplets ejected into water during the piercing of the oil-water interface by the liquid jet. Regardless of the location of the bubble collapse, be it in the oil phase or the water phase, the bubble always moves in the direction of jet upon collapsing, which has been observed in the previous recording sequence and confirmed in this case. Simulated sequence in Fig. 19 ends after the second bubble's rebound, when the bubble is about to penetrate the interface, due to numerical constraints explained in Sec. 2.2. Up to that point the simulated sequence nicely matches

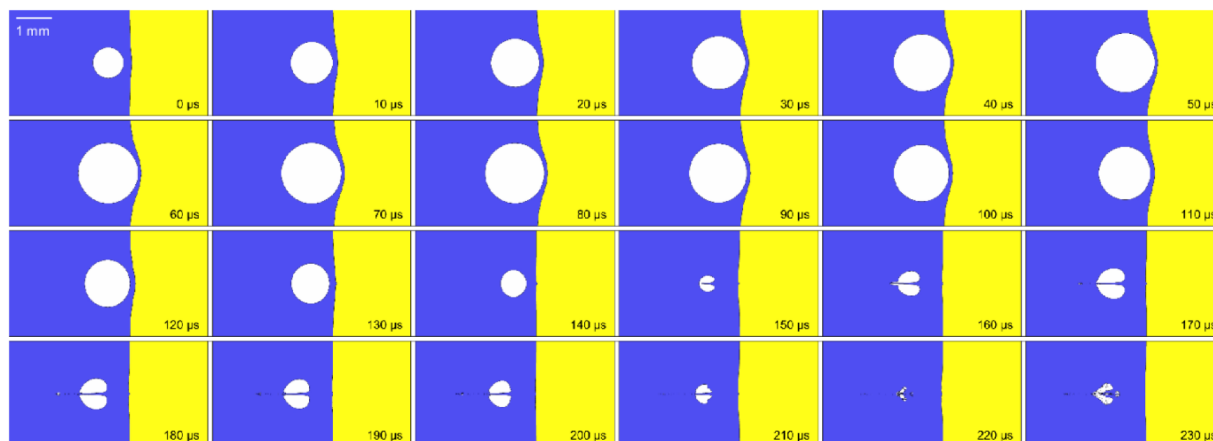


Fig. 11. Bubble evolution in water at $\gamma = 0.7$. and $\zeta = 0.016$, numerical simulation.

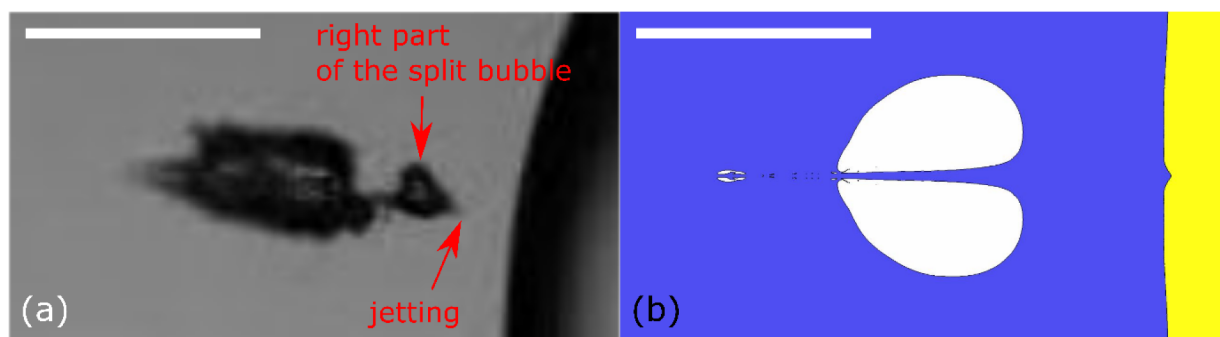


Fig. 12. (a) Experimental detail of a split cavitation bubble at 170 μs of the recorded sequence with the jet appearing also on the smaller right part of the split bubble and (b) numerical simulation frame at the same time showing no bubble splitting.

experimental observation. The jet in the simulated sequence has a relatively far reach of about one maximum bubble radius. This cannot be seen in the experimental sequence, probably because the jet is unable to pull the bubble with it due to the small pierced area in the interface.

3.4. Bubble collapse at the liquid–liquid interface ($\gamma = 0.2$ & 0.01 , $\zeta = 0.2$ & -8.1)

3.4.1. Bubble in water

The bubble in Fig. 20 was generated in water at $\gamma = 0.2$, $\zeta = 0.2$. Fig. 21 shows the corresponding numerical simulation sequence.

Behaviour of the cavitation bubble is similar to one in case of $\gamma = 0.7$ and 0.5 . It is evident from frames 160 μs to 240 μs in Fig. 20 that a small bump appears on the water–oil interface when the jet penetrates the bubble. This phenomenon is also supported by numerical simulations, as can be seen in Fig. 21. The deformation of the interface can be attributed to the shear flow along the interface and through the bubble, when a collapsing bubble detaches from the oil phase and develops a primary jet away from the interface (see Fig. 21 at 140 and 150 μs). A small part of the bubble towards the water–oil interface is impinged upon the collapse, which results in a secondary jet towards the interface. This detail is emphasized in Fig. 22 with (a) showing experimental observation and (b) corresponding simulated frame.

3.4.2. Bubble in oil

The bubble in Fig. 23 was generated in oil at $\gamma = 0.01$, $\zeta = -8.1$.

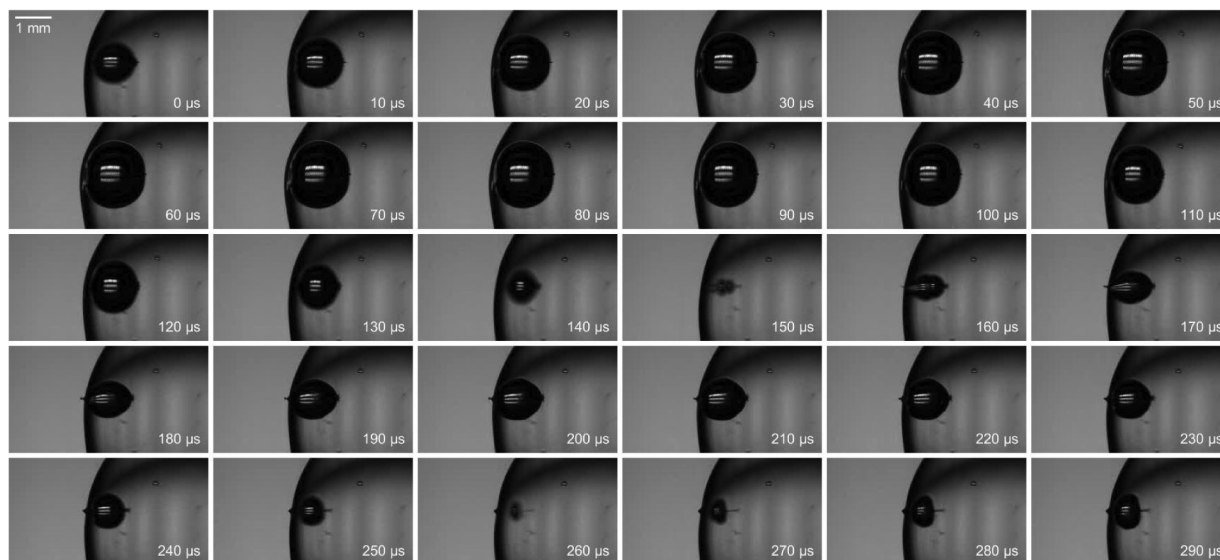


Fig. 13. Bubble evolution in oil at $\gamma = 0.7$ and $\zeta = -0.016$, experimental observation.

Fig. 24 shows the numerical simulation sequence.

In this case the bubble is generated almost on the oil–water interface, slightly inside the oil phase. The interface is penetrated by the jet during first collapse and the bubble is transferred into the water phase. No jet is visible at the second bubble collapse, however a slight pull of the oil boundary can be noticed at 300 μs and later in Fig. 23 as well as in numerical simulation (Fig. 24). The oil, which is pulled from the boundary during the collapse, is then further smeared in the form of many small oil droplets over the area around cavitation bubble. In this example simulated sequence is able to demonstrate the transfer of the cavitation bubble from the oil to water phase due to the smaller γ and thus faster transfer time. Jetting is seen in simulated sequence in Fig. 24 also at the second collapse, while circumstances in experimental sequence are too unclear to confirm the simulation.

In the case of experiment the plasma was created just about 10 μm inside the oil droplet, hence it is likely that there is some interaction between it and the interface. However it seems to be small, because the “trend” of the physics is not altered at all (we see very similar events as in the case of $\gamma = 0.5$, where there is surely no interaction between the plasma and the interface).

4. Discussion

In the following section we show quantitative analysis of various parameters as a function of the anisotropy parameter ζ . In the analysis, both experiments and simulations are considered. Bubble radii (R_{max} ,

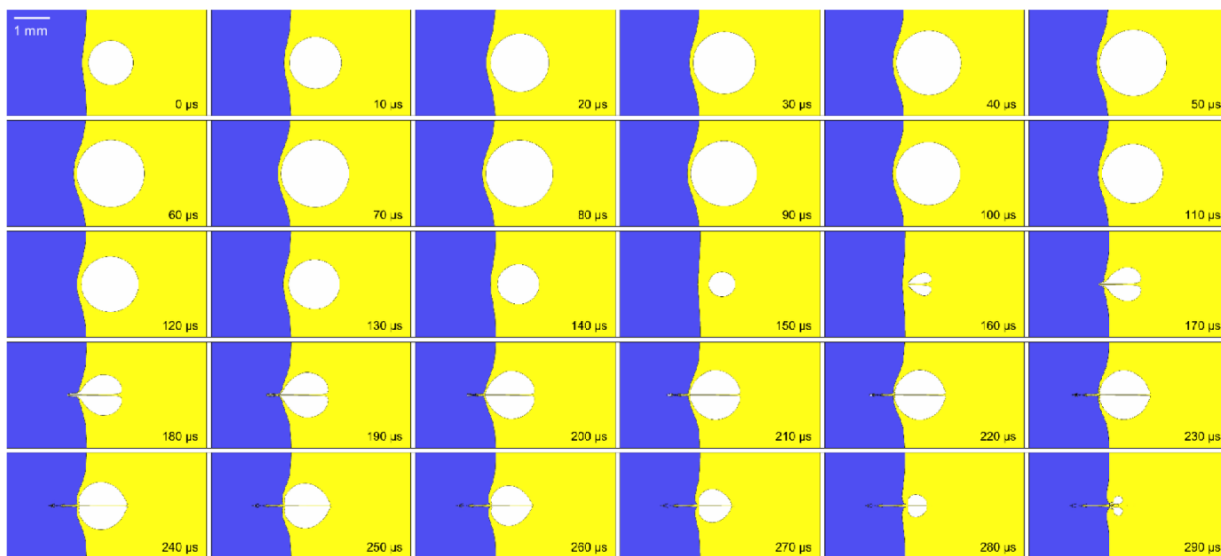


Fig. 14. Bubble evolution in oil at $\gamma = 0.7$ and $\zeta = -0.016$, numerical simulation.

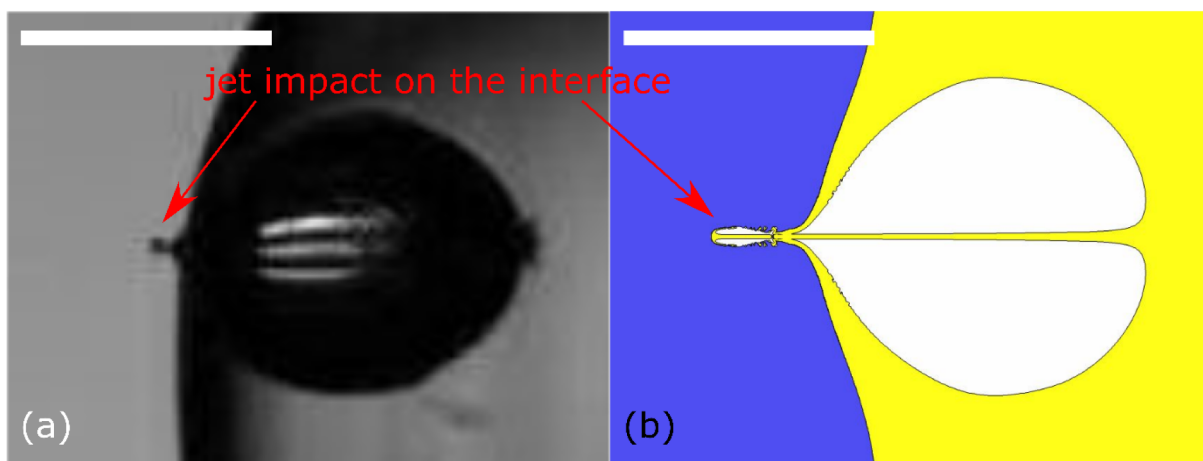


Fig. 15. (a) Recorded detail of a jet impact on the water-oil interface manifested as a small bump and (b) the same phenomena confirmed by numerical simulation.

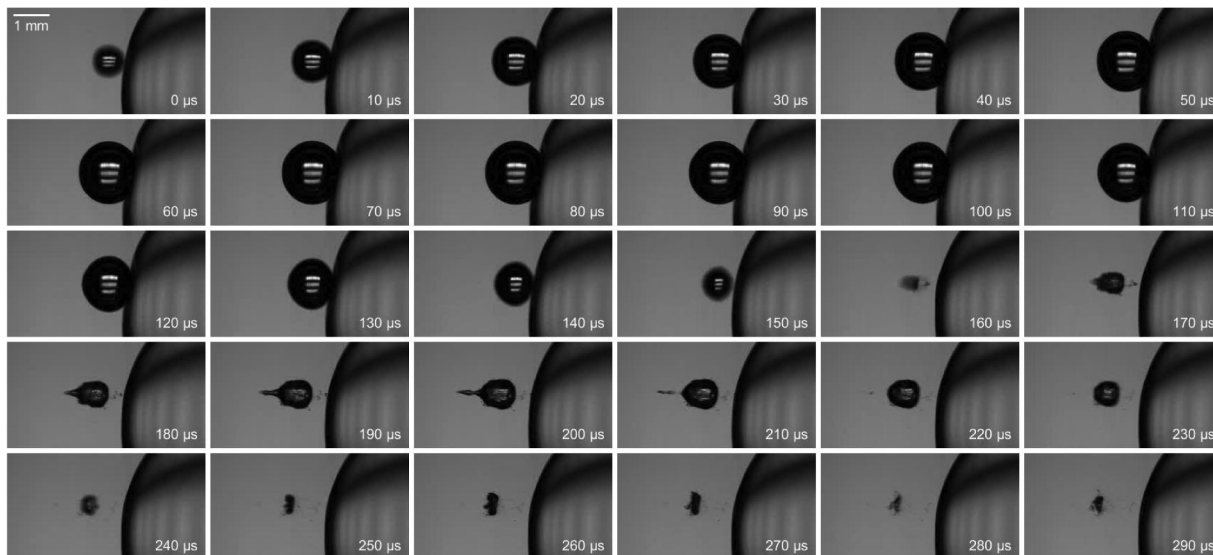


Fig. 16. Bubble evolution in water at $\gamma = 0.5$ and $\zeta = 0.032$, experimental observation.

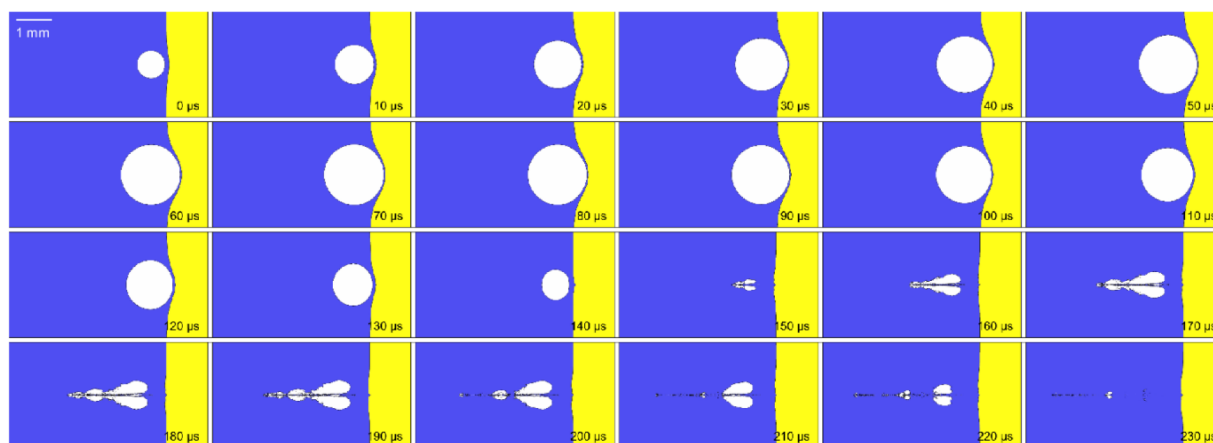


Fig. 17. Bubble evolution in water at $\gamma = 0.5$, and $\zeta = 0.032$, numerical simulation.

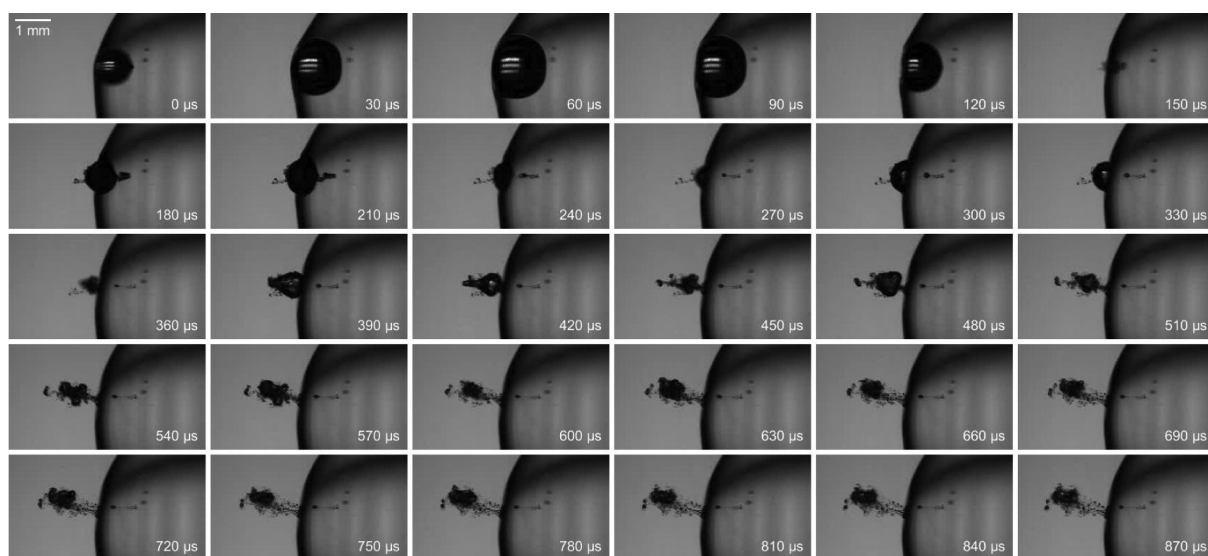


Fig. 18. Bubble evolution in oil at $\gamma = 0.5$ and $\zeta = -0.032$, experimental observation.

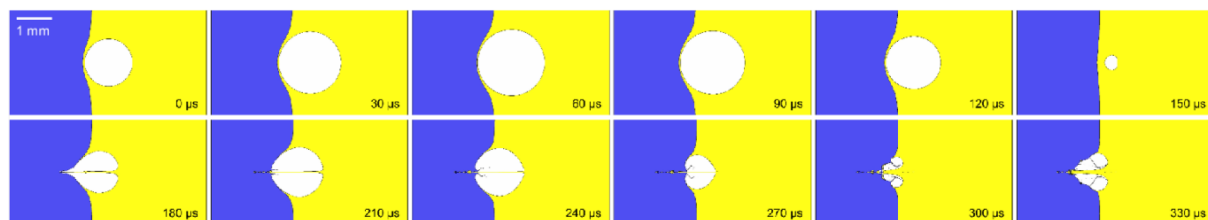


Fig. 19. Bubble evolution in oil at $\gamma = 0.5$ and $\zeta = -0.032$, numerical simulation until the second bubble rebound.

$R_{\max,2}$) were determined by measuring bubble size in lateral and longitudinal directions and averaging it, or, in the case of very small and deformed bubble (just before and after the collapse) we determined it by measuring the area it occupies in the picture and derived the corresponding equivalent (spherical) radius from it.

Finally, we also discuss the possible implications of the present study for the understanding of the ultrasonic emulsification process.

Firstly, we evaluated the displacement of the bubble after the collapse. Clearly, as predicted by the anisotropy parameter ζ the bubble, which collapses in the vicinity of the liquid–liquid interface, will always jet towards the denser liquid. We show in Fig. 25 the normalized bubble

centroid displacement ($\Delta x/R_{\max}$) as a function of an anisotropy parameter ζ . Positive values of displacement imply movement away from the interface and negative values towards the interface. Absolute values for ζ are given in x-axis.

At very small ζ values we are dealing with almost spherical bubble and it remains stagnant ($\Delta x/R_{\max} \approx 0$). Obviously, the bubble moves in the same direction as it jets. Bubble in oil moves towards the interface and even traverses it (for example Figs. 18 and 23). On the other hand, the bubble in water jets and moves away from the interface. The displacement increases with increasing anisotropy parameter ζ (with decreasing initial distance of bubble from the interface). A similar

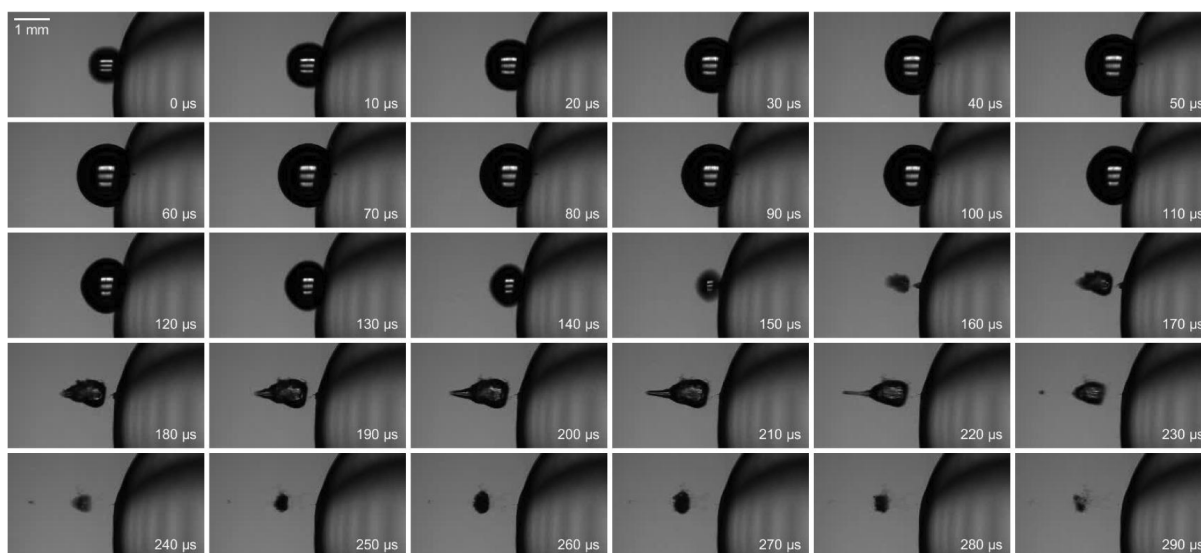


Fig. 20. Bubble evolution in water at $\gamma = 0.2$, and $\zeta = 0.2$, experimental observation.

conclusion was already found and reported by Supponen [17]. Interestingly, we find that the trend, in an absolute sense, is almost identical for bubble on either side of the interface and clearly follows a logarithmic-law fit (the values of the coefficients of the logarithmic function fits are almost identical in an absolute sense).

The logarithmic fits seem to describe the movement well in the range between $10^{-3} < |\zeta| < 10$. At smaller values the displacement would remain at 0 (increasingly more symmetrical bubble, and consequently no displacement). What occurs at higher values of anisotropy parameter is not certain, but the interaction of the bubble with the interface would surely distort the curve.

The results (trends) are in line with the work by Supponen [17] although they measure the displacements to be somewhat larger, which may be due to the much larger bubbles used in their experimental campaign.

Fig. 26 shows the dependence of the maximal size of the rebounded bubble $R_{\max,2}$ – again we show normalized values $R_{\max,2}/R_{\max,1}$.

Values for bubble in oil at $\zeta = -0.2$ and -8.1 are not included in the diagram, since the bubble traverses the interface and the rebound occurs inside water (Figs. 18 and 23). Similarly, the logarithmic fits cannot be considered beyond $|\zeta| > 0.2$. As one might expect, by increasing the bubble-fluid interface distance γ and thus decreasing the anisotropy parameter ζ , the relative rebound radii approach the

corresponding values for an unbounded bubble, with $R_{\max,2}/R_{\max,1} \sim 0.33$ and 0.70 in water and oil, respectively.

One notices that the magnitude of a rebound seems to increase with ζ . This can be explained by the fact, that the collapsing bubbles tend to progressively deviate from their initial spherical shape with stronger influence of jet drivers. This translates to increasingly more pronounced asymmetric bubble behaviour, which results in larger bubble radius at the point of collapse – consequently the shock wave amplitude decreases, leaving more energy to drive the secondary bubble expansion to a larger volume. This is also supported by the numerical results shown in Fig. 27, where temporal maximums of averaged pressures at the distance of R_{\max} from the initial bubble centre are given.

One can notice that the shockwave pressure decreases exponentially with the increasing anisotropy ζ , leaving more energy for the consequent bubble rebound.

Due to a very different dynamics of bubbles in water and oil it is hard to obtain reliable data on the velocities that the jets develop. Also, the jet length is of a greater interest as the study can be applied to the emulsification process physics. Fig. 28 shows the results of the normalized jet length (jet length divided by the current bubble radius L/R) as a function of anisotropy parameter.

Of course, the bubble does not develop a jet at a low value of anisotropy, but already at a relatively weak influence of the interface the

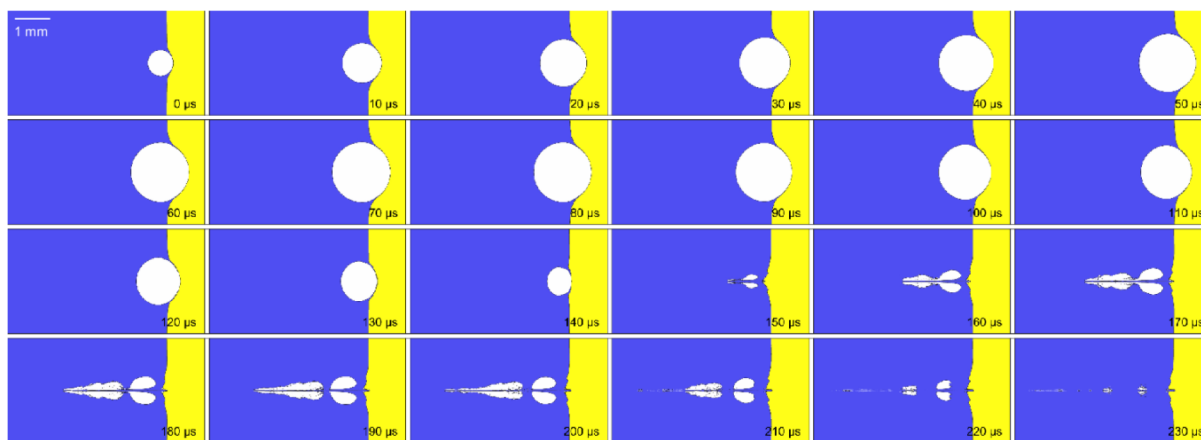


Fig. 21. Bubble evolution in water at $\gamma = 0.2$, and $\zeta = 0.2$, numerical simulation.

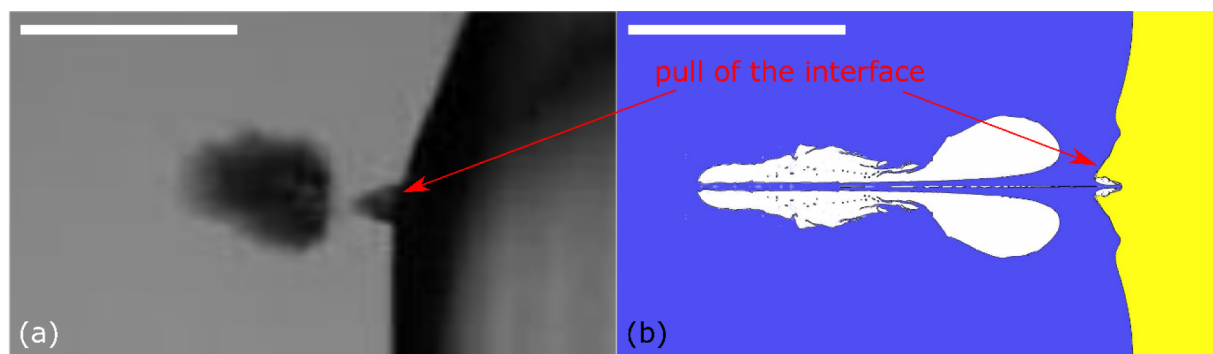


Fig. 22. (a) Experimental detail during the jet phase of the bubble dynamics, namely a bump on the interface due to low pressure are behind the jet and (b) numerical simulation of the same phenomena.

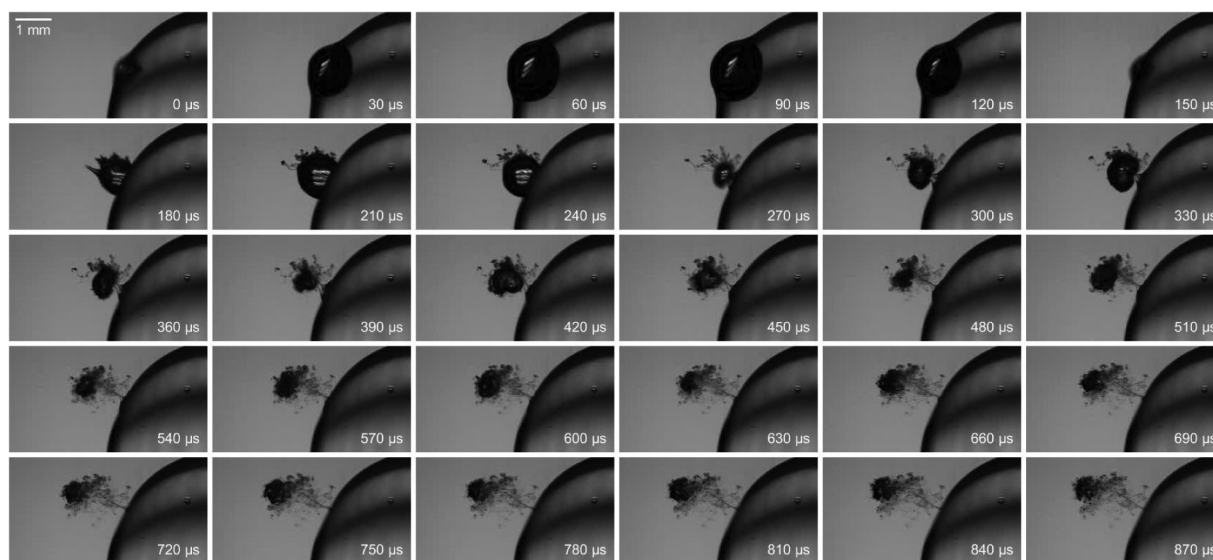


Fig. 23. Bubble evolution in oil at $\gamma = 0.01$ and $\zeta = -8.1$, experimental observation.

bubble jets. The jetting becomes more significant when the interface is in vicinity. The relationship is the same for bubble in water and in oil, however the one in oil is less pronounced. This is of course due to the fact that it moves towards the interface and the denser liquid, what influences the overall bubble dynamics - the collapse is a bit slower and the bubble is deformed more in the lateral direction (compare for example Figs. 10 and 13).

Values for bubble in oil at $\zeta = -0.2$ and -8.1 are again not included in the diagram, since the bubble traverses the interface it is impossible to determine the jet length (Figs. 18 and 23). Similarly, the logarithmic fits cannot be considered beyond $|\zeta| > 0.03$ (oil) and $|\zeta| > 0.2$ (water).

Besides the fundamental aspect, the present work also has an applied value – namely understanding the physics of emulsification by

ultrasound. In [1] we observed that the process begins with water penetrating the bulk oil phase (Fig. 29).

We observe oil–water interface, visible as the curved line. Additionally, the cavitation bubbles are visible on the right side of the interface, inside the water phase. The following frames (Fig. 29, Frames b) to d)) show, how the cavitation bubbles appear near the interface.

In Fig. 29, Frames c) to j) we can observe the water introduction into the bulk oil phase. This is visible as the appearance and growth of a mushroom shaped structure. Looking at the present experiments and simulations, we know that the bubble will always jet away from the less dense liquid... in the present case of a bubble created inside water, it will jet away from the interface. This results in the fact that the water is penetrating the oil not due to the jetting, but likely as a result of acoustic streaming of nuclei towards the interface as a result of primary

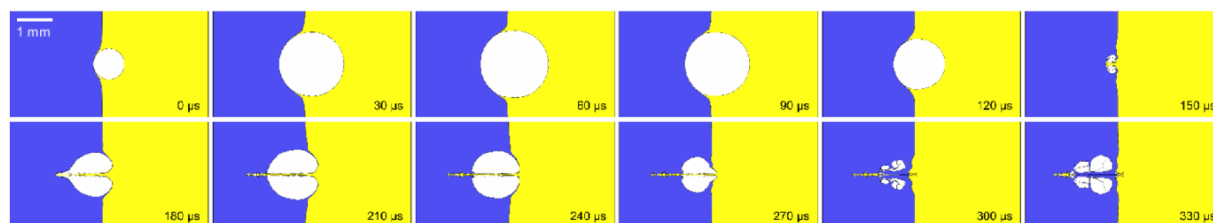


Fig. 24. Bubble evolution in oil at $\gamma = 0.2$ and $\zeta = -0.2$, numerical simulation until the second bubble rebound.

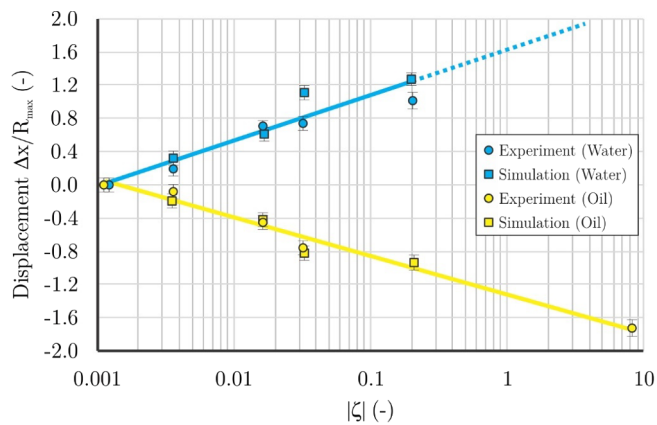


Fig. 25. Normalized bubble centroid displacement ($\Delta x/R_{max}$) as a function of an anisotropy parameter $|\zeta|$. Solid lines are fit functions: $\Delta x/R_{max} = 0.1152 \cdot \ln(|\zeta|) + 0.7959$ and $\Delta x/R_{max} = -0.1004 \cdot \ln(|\zeta|) - 0.6639$, for water and oil, respectively.

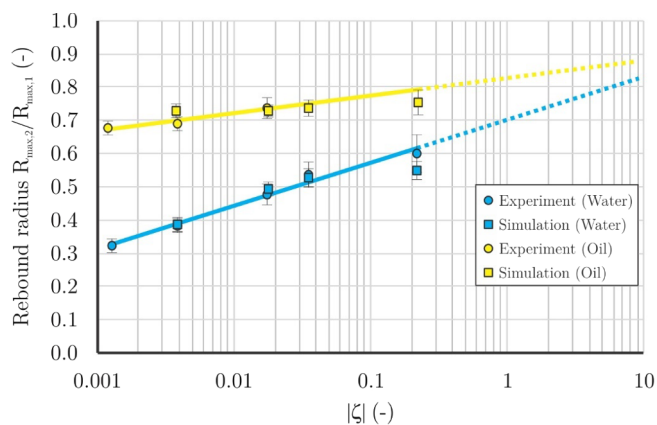


Fig. 26. Normalized maximal size of the rebounded bubble ($R_{max,2}/R_{max,1}$) as a function of an anisotropy parameter $|\zeta|$. Solid lines are fit functions: $R_{max,2}/R_{max,1} = 0.0139 \cdot \ln(|\zeta|) + 0.7894$ and $R_{max,2}/R_{max,1} = 0.0506 \cdot \ln(|\zeta|) + 0.6844$, for water and oil, respectively.

Bjerknes force [15,16].

The other occasion where a single bubble plays a role in emulsification is later on, when large droplets of oil enter the bulk water phase, due to the Rayleigh Taylor instability (Fig. 30). Experiments have shown that these can already be treated as partial emulsions and contain a large quantity of cavitation nuclei.

Likely the bubble will grow inside them and collapse, this time (according to the present study) jetting towards the interface and producing a fine oil in water emulsion (see for example Figs. 18 and 23 in the present study). This process was also observed in experiments by ultrasonic cavitation, what is shown in Fig. 31 (from [1]).

5. Conclusions

In our previous work [1] we pointed out that it is essential, for later optimization of the emulsification process, to firstly understand the interaction between single bubbles and the liquid–liquid interface. However, a literature survey revealed that, apart from the work by Chahine & Bovis [29], no thorough work was done on this topic.

In the present work we show a number of experiments where single cavitation bubble dynamics was observed on each side of the oil–water

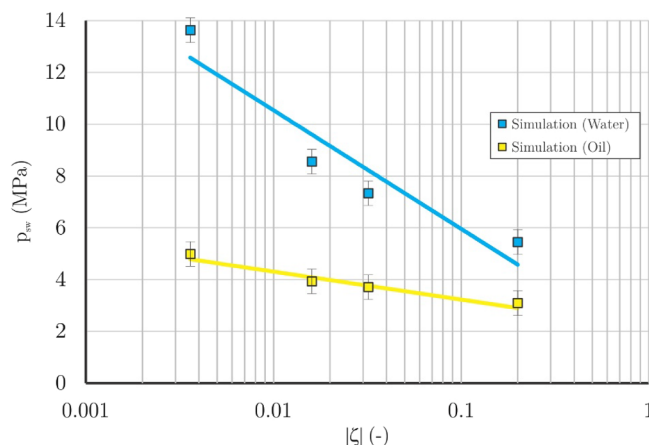


Fig. 27. Temporal maximums of averaged pressures at radial distance $R = R_{max}$ from the initial bubble center as a function of an anisotropy parameter $|\zeta|$. Solid lines are fit functions: $p_{sw} = -1.988 \cdot \ln(|\zeta|) + 1.3762$ and $p_{sw} = -0.465 \ln(|\zeta|) + 2.2118$, for water and oil, respectively.

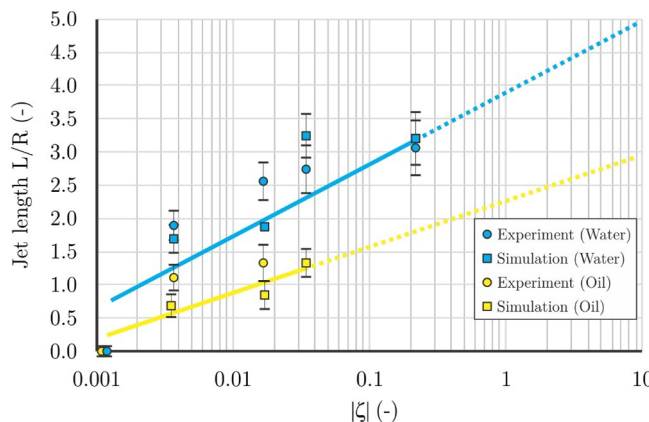


Fig. 28. Normalized jet length (L/R) as a function of an anisotropy parameter $|\zeta|$. Solid lines are fit functions: $L/R = 0.4628 \cdot \ln(|\zeta|) + 3.9062$ and $L/R = 0.2973 \cdot \ln(|\zeta|) + 2.2718$, for water and oil, respectively.

interface. To be able to investigate in detail on how the bubble interacts with the interface, the experiments were complemented by numerical simulations. It is revealed that the bubble always jets toward the interface if it grows in the lighter liquid and correspondingly away from the interface if it is initiated inside the denser liquid. This is also predicted by the anisotropy parameter, which was introduced by Suponnen et al. [17]. The relationship between the anisotropy parameter and the characteristics of bubble jetting was also investigated.

Based on the present study of single bubble interaction with liquid–liquid interface, we were able to give more in depth explanations on the dynamics of multiple ultrasonically induced bubbles, which we observed in our previous work on ultrasonic emulsification [1]. The present study also implies that that efficient emulsification can only be achieved when the bubbles jets towards the interface, hence they must be created inside the lighter (oil) phase. On an applied level this can only be achieved by an ultrasonic horn with the tip inside the oil phase. Surely the gained deeper understanding of the bubble dynamics and emulsification physics will lead to optimization of the industrial emulsification processes in the future.

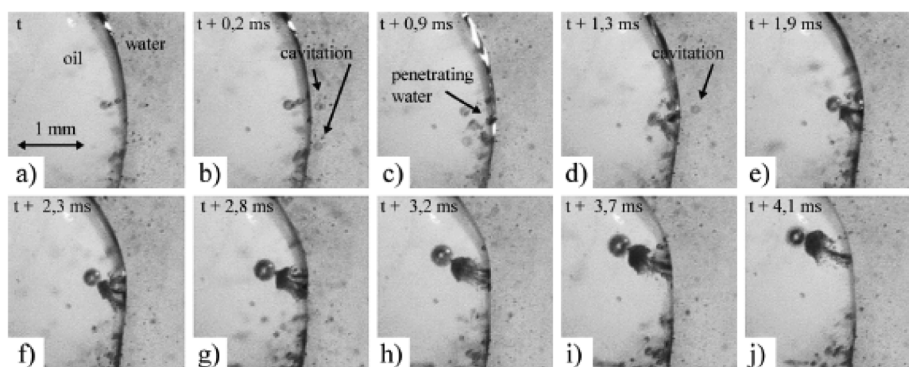


Fig. 29. Oil water interface in an ultrasonic field. Cavitation bubble forms inside water and pushes water into the oil bulk phase (from [1]).

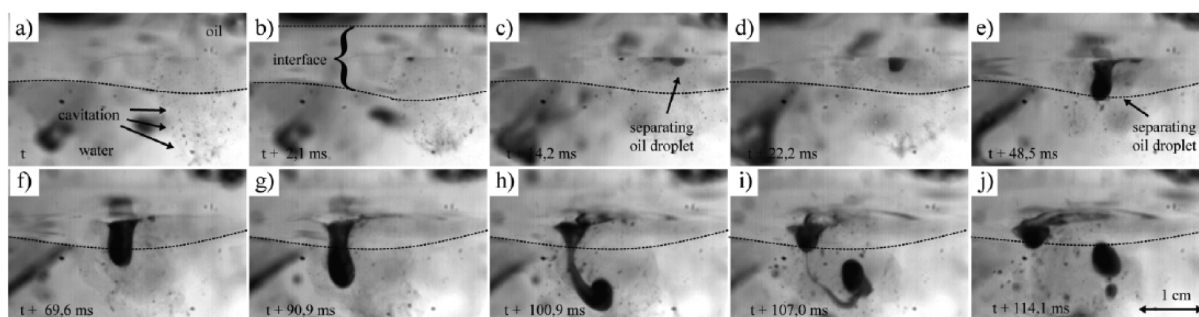


Fig. 30. Separation of the partial emulsion droplet due to the Rayleigh Taylor instability (from [1]).

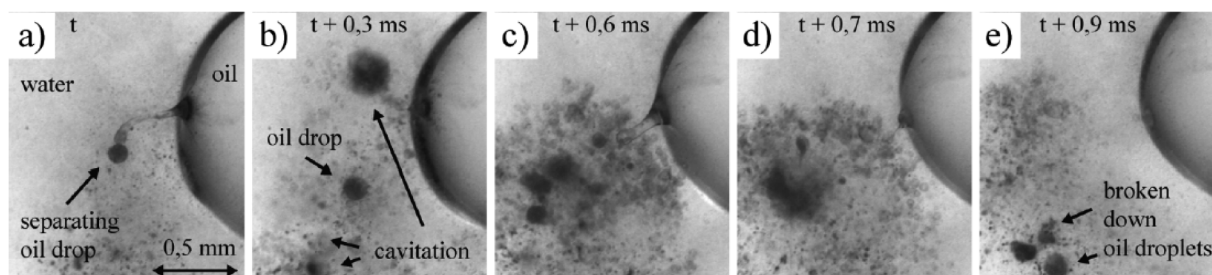


Fig. 31. Disruption of the droplet containing partial emulsion due to cavitation (from [1]).

CRedit authorship contribution statement

Uroš Orthaber: Investigation, Writing - original draft, Writing - review & editing. **Jure Zevnik:** Investigation, Writing - review & editing. **Rok Petkovšek:** Methodology, Supervision, Writing - original draft, Writing - review & editing. **Matevž Dular:** Conceptualization, Visualization, Writing - review & editing, Supervision.

Declaration of Competing Interest

The authors declare that they have no known competing financial interests or personal relationships that could have appeared to influence the work reported in this paper.

Acknowledgments

The authors acknowledge the financial support from the Slovenian Research Agency (research core Funding No. P2-0401, No. P2-0270 and Projects BI-US/18-19-031), from the Ministry of Education, Science and Sport (contract # C-3330-17-529029) and the European Research Council (ERC) under the European Union's Framework Program for research and innovation, Horizon 2020 (grant agreement n° 771567 — CABUM)

References

- [1] T.S. Perdih, M. Zupanc, M. Dular, Revision of the mechanisms behind oil-water (O/W) emulsion preparation by ultrasound and cavitation, *Ultrason. - Sonochem.* 51 (September 2018) (2019) 298–304, <https://doi.org/10.1016/j.ulsonch.2018.10.003>.
- [2] F. Reuter, H. Sagar, R. Mettin, Wall, shear rates induced by a single cavitation bubble collapse, *Proc. 10th Int. Symp. Cavitation* (2018).
- [3] M. Dular, T. Požar, J. Zevnik, R. Petkovšek, High speed observation of damage created by a collapse of a single cavitation bubble, *Wear* 418–419 (2019) 13–23, <https://doi.org/10.1016/j.wear.2018.11.004>.
- [4] K.S. Suslick, *Sonochemistry, Science* (80-) 247 (4949) (1990) 1439–1445, <https://doi.org/10.1126/science.247.4949.1439>.
- [5] V. Agrez, T. Pozar, R. Petkovšek, High-speed photography of shock waves with an adaptive illumination, *Opt. Lett.* 45 (6) (2020) 1547–1550, <https://doi.org/10.1364/OL.388444>.
- [6] A. Sarc, M. Oder, M. Dular, Can rapid pressure decrease induced by supercavitation efficiently eradicate *Legionella pneumophila* bacteria? *Desalin. Water Treat.* 57 (5) (2016) pp, <https://doi.org/10.1080/19443994.2014.979240>.
- [7] H. Shamsborhan, O. Coutier-Delgosha, G. Caignaert, F. Abdel, Nour, “Experimental determination of the speed of sound in cavitating flows”, *Exp. Fluids* 49 (6) (2010) 1359–1373, <https://doi.org/10.1007/s00348-010-0880-6>.
- [8] A. Šarc, J. Kosel, D. Stopar, M. Oder, M. Dular, Removal of bacteria *Legionella pneumophila*, *Escherichia coli*, and *Bacillus subtilis* by (super)cavitation, *Ultrason. Sonochem.* 42 (2018), <https://doi.org/10.1016/j.ulsonch.2017.11.004>.
- [9] P.R. Gogate, Cavitation reactors for process intensification of chemical processing applications: A critical review, *Chem. Eng. Process. Process Intensif.* 47 (4) (2008) 515–527, <https://doi.org/10.1016/j.cep.2007.09.014>.
- [10] M. Zupanc, et al., Removal of pharmaceuticals from wastewater by biological processes, hydrodynamic cavitation and UV treatment, *Ultrason. Sonochem.* 20 (4)

- (2013) 1104–1112, <https://doi.org/10.1016/j.ultsonch.2012.12.003>.
- [11] P.R. Gogate, A.B. Pandit, A review of imperative technologies for wastewater treatment I: oxidation technologies at ambient conditions, *Adv. Environ. Res.* 8 (3) (2004) 501–551, [https://doi.org/10.1016/S1093-0191\(03\)00032-7](https://doi.org/10.1016/S1093-0191(03)00032-7).
- [12] M. Dular, et al., Use of hydrodynamic cavitation in (waste)water treatment, *Ultrason. Sonochem.* 29 (2016) 577–588, <https://doi.org/10.1016/j.ultsonch.2015.10.010>.
- [13] R. Ciriminna, L. Albanese, V. Di Stefano, R. Delisi, F. Meneguzzo, M. Pagliaro, Beer produced via hydrodynamic cavitation retains higher amounts of xanthohumol and other hops prenylflavonoids, *LWT* 91 (2018) 160–167.
- [14] J. Carpenter, M. Badve, S. Rajoriya, S. George, V.K. Saharan, A.B. Pandit, Hydrodynamic cavitation: An emerging technology for the intensification of various chemical and physical processes in a chemical process industry, *Rev. Chem. Eng.* 33 (5) (Oct. 2017) 433–468, <https://doi.org/10.1515/revce-2016-0032>.
- [15] I. Tzanakis, G.S.B. Lebon, D.G. Eskin, K.A. Pericleous, Characterizing the cavitation development and acoustic spectrum in various liquids, *Ultrason. Sonochem.* (2017), <https://doi.org/10.1016/j.ultsonch.2016.06.034>.
- [16] A.A. Doinikov, Bjerknes forces and translational bubble dynamics, *Bubble and Particle Dynamics in Acoustic Fields: Modern Trends and Applications*, Research Signpost, 2005, pp. 95–143.
- [17] O. Supponen, D. Obreschkow, M. Tinguely, P. Kobel, N. Dorsaz, M. Farhat, Scaling laws for jets of single cavitation bubbles, *J. Fluid Mech.* 802 (2016) 263–293, <https://doi.org/10.1017/jfm.2016.463>.
- [18] A.M. Zhang, S. Li, J. Cui, Study on splitting of a toroidal bubble near a rigid boundary, *Phys. Fluids* (2015), <https://doi.org/10.1063/1.4922293>.
- [19] O. Supponen, D. Obreschkow, P. Kobel, M. Tinguely, N. Dorsaz, M. Farhat, Shock waves from nonspherical cavitation bubbles, *Phys. Rev. Fluids* (2017), <https://doi.org/10.1103/PhysRevFluids.2.093601>.
- [20] R.P. Tong, W.P. Schiffers, S.J. Shaw, J.R. Blake, D.C. Emmony, The role of ‘splashing’ in the collapse of a laser-generated cavity near a rigid boundary, *J. Fluid Mech.* (1999), <https://doi.org/10.1017/S0022112098003589>.
- [21] M.P. Brenner, S. Hilgenfeldt, D. Lohse, Single-bubble sonoluminescence, *Rev. Modern Phys.* (2002), <https://doi.org/10.1103/RevModPhys.74.425>.
- [22] T.B. Benjamin, A.T. Ellis, The collapse of cavitation bubbles and the pressures thereby produced against solid boundaries, *Philos. Trans. R. Soc. London. Ser. A, Math. Phys. Sci.* 260 (1110) (1966) 221–240 [Online]. Available: <http://www.jstor.org/stable/73553>.
- [23] J.R. Blake, The Kelvin impulse: application to cavitation bubble dynamics, *J. Aust. Math. Soc. Ser. B. Appl. Math.* (1988), <https://doi.org/10.1017/s0334270000006111>.
- [24] J.R. Blake, D.M. Leppinen, Q. Wang, Cavitation and bubble dynamics: The Kelvin impulse and its applications, *Interface Focus* (2015), <https://doi.org/10.1098/rsfs.2015.0017>.
- [25] M. Dular, T. Pozar, J. Zevnik, R. Petkovsek, High speed observation of damage created by a collapse of a single cavitation bubble, *Wear* 419 (Jan) (2019) 13–23, <https://doi.org/10.1016/j.wear.2018.11.004>.
- [26] J.-C. Isselin, A.-P. Alloncle, M. Autric, On laser induced single bubble near a solid boundary: Contribution to the understanding of erosion phenomena, *J. Appl. Phys.* 84 (10) (1998) 5766–5771, <https://doi.org/10.1063/1.368841>.
- [27] M.S. Plesset, R.B. Chapman, Collapse of an initially spherical vapour cavity in the neighbourhood of a solid boundary, *J. Fluid Mech.* 47 (02) (1971) 283, <https://doi.org/10.1017/S0022112071001058>.
- [28] J.R. Blake, D.C. Gibson, Cavitation bubbles near boundaries, *Annu. Rev. Fluid Mech.* 19 (1) (1987) 99–123, <https://doi.org/10.1146/annurev.fl.19.010187.000531>.
- [29] G.L. Chahine, A. Bovis, *Oscillation and collapse of a cavitation bubble in the vicinity of a two-liquid interface, Cavitation and Inhomogeneities in Underwater Acoustics*, Springer Berlin Heidelberg, Berlin, Heidelberg, 1980, pp. 23–29.
- [30] Y. Tomita, P.B. Robinson, R.P. Tong, J.R. Blake, Growth and collapse of cavitation bubbles near a curved rigid boundary, *J. Fluid Mech.* (2002), <https://doi.org/10.1017/S0022112002001209>.
- [31] F. Mohamed, O. Danail, K. Philippe, D. Nicolas, D.B. Aurel, Interaction of a cavitation bubble with a spherical free surface, *Water* (2006).
- [32] I. ANSYS, “Fluent 20.1 manual.” 2020.
- [33] M. Koch, C. Lechner, F. Reuter, K. Köhler, R. Mettin, W. Lauterborn, Numerical modeling of laser generated cavitation bubbles with the finite volume and volume of fluid method, using OpenFOAM, *Comput. Fluids* 126 (2016) 71–90, <https://doi.org/10.1016/j.compfluid.2015.11.008>.
- [34] A. Osterman, M. Dular, B. Širok, Numerical simulation of a near-wall bubble collapse in an ultrasonic field, *J. Fluid Sci. Technol.* 4 (1) (2009) 210–221, <https://doi.org/10.1299/jfst.4.210>.
- [35] P. Koukouvinis, M. Gavaises, O. Supponen, M. Farhat, Numerical simulation of a collapsing bubble subject to gravity, *Phys. Fluids* 28 (3) (2016), <https://doi.org/10.1063/1.4944561>.
- [36] B. Han, K. Köhler, K. Jungnickel, R. Mettin, W. Lauterborn, A. Vogel, Dynamics of laser-induced bubble pairs, *J. Fluid Mech.* 771 (2015) 706–742, <https://doi.org/10.1017/jfm.2015.183>.
- [37] C. Lechner, M. Koch, W. Lauterborn, R. Mettin, Pressure and tension waves from bubble collapse near a solid boundary: A numerical approach, *J. Acoust. Soc. Am.* 142 (6) (2017) 3649–3659, <https://doi.org/10.1121/1.5017619>.
- [38] I. Akhatov, O. Lindau, A. Topolnikov, R. Mettin, N. Vakhitova, W. Lauterborn, Collapse and rebound of a laser-induced cavitation bubble, *Phys. Fluids* (2001), <https://doi.org/10.1063/1.1401810>.